RSC Advances

ROYAL SOCIETY OF CHEMISTRY

www.rsc.org/advances

Effects of structural, optical and ferromagnetic states on the photocatalytic activities of Sn-TiO_2 nanocrystals

Ayyakannu Sundaram Ganeshraja[a,b], Subramani Thirumurugan[b,‡], Kanniah Rajkumar[b,‡], Kaixin Zhu [a,c], Yanjie Wang[a,c], Krishnamoorthy Anbalagan[b*], Junhu Wang[a*]

[a] *Mössbauer Effect Data Center, Dalian Institute of Chemical Physics, Chinese Academy of Science, Dalian 116023, China*

E-mail: wangjh@dicp.ac.cn ; Tel: +86 411 84379159

[b] *Department of Chemistry, Pondicherry University, Pondicherry 605014, India*

E-mail: kanuniv@gmail.com; Tel: +91 413 2654509

[c] *University of Chinese Academy of Sciences, Beijing 100049, China*

‡These authors contributed equally to this work

Abstract

The structural, electronic, magnetic and photocatalytic properties of Sn doped TiO_2 diluted magnetic semiconductor nanoparticles (NPs) prepared by a simple hydrothermal method were systematically investigated by various conventional techniques and ^{119}Sn Mössbauer spectroscopy. Anatase, mixture (anatase-rutile) and rutile phases of Sn-TiO_2 NPs were obtained by adding different amounts of $SnCl_4$ into a titanium nitrate aqueous solution. Photocatalytic degradation of methyl orange and phenol derivatives (*R*PhOH) were studied under visible and UV light irradiation in

water, respectively. The photocatalytic activities of prepared NPs were found to be drastically related with the structural, optical and ferromagnetic properties. Significant relation was observed between the Hammett substitution constants of *R*PhOH and the photocatalytic activities. Among all the samples, anatase phase with low Sn contents performed better photocatalytic and ferromagnetic characters at room temperature.

Key words: Hydrothermal method, Sn doped and coupled TiO_2, Room temperature ferromagnetism, Photocatalysis, Hammett's substitution constant

1. Introduction

Metal oxide semiconductors such as TiO_2, SnO_2, and ZnO have been commonly regarded as benchmark photocatalysts and their role in the relevant area has been substantially studied for several decades. They show special properties such as enhanced photoluminescence, chemical and photochemical reactivities.[1-3] Since the study of TiO_2 has become such a widespread and multidisciplinary field, a significant amount of research has been dedicated in the past.[4-6] The photocatalytic activity of TiO_2 has been shown to be dependent on several key factors: crystal phase, surface area, exposed crystal facets, uncoordinated surface sites, defects in the lattice, and degree of crystallinity. Additionally, metal doped TiO_2 nanoparticles (NPs) can create and tune other properties such as mid-band-gap electronic states which can alter charge migration or produce a red shift in the absorption spectrum. More emphasis has been paid on SnO_2-TiO_2 system in the recent years by integrating together both

the properties of the two oxides. It is generally accepted that the new nanocomposite exhibits higher photocatalytic reactivity compared with pure titania.[7] The SnO_2-TiO_2 nanocomposites could be fabricated by the simple hydrothermal method and small variations in the conditions of synthesis are possible to lead to the production of distinct materials.[8] Cao et al.[9] reported that Sn^{4+} ions could be doped into TiO_2 lattice in substitutional mode and/or exist in the form of $SnCl_x$ or tin oxide, which depends on the annealing temperature. Wang et al.[10] reported that Sn-TiO_2 and Sn-Fe-TiO_2 resulted in a red-shift of the optical absorption edge of TiO_2; most of the Sn 5*s* states were suggested to locate at the bottom of the conduction band and hybrid with the Ti 3*d* states.

Meanwhile, ferromagnetism in diluted magnetic semiconductors (DMS) has been another important subject of great scientific and technological interest for the past few years due to the possibility of manipulating charge and spin degrees of freedom.[11] In particular, room-temperature ferromagnetic (RTFM) oxides have attracted great attention from magnetic fluids, biomedicine, magnetic resonance imaging, catalysis, and environmental remediation.[12] Wang et al.[13] developed a simple method to fabricate ZnO crystals with abundant Zn vacancies, and observed p-type conductivity, RTFM, and excellent photocatalytic activity. Anbalagan[14] and Ganeshraja[15] reported the ferromagnetic ordering in transition metal such as Co / Fe / Zn doped TiO_2 NPs could be justified by the creation of some defect sites in the samples. The Sn-TiO_2 NPs were also found to have RTFM property; however, the actual role of *p*-block element, in the present investigation, tin is still unclear.[16]

Very recently, we reported the ferromagnetism and photocatalytic activity in metal oxide coupled nanocomposites.[17] The photocatalytic activity and magnetism studies of prepared metal oxide coupled nanocomposites might suggest a major role of surface oxygen vacancies and charge carriers.[18] The RTFM nanocomposites were found to show better photocatalytic performance instead of diamagnetic commercially available photocatalysts under visible light irradiation.[17,19] In order to take high activity of the coupled,[19] doped or co-doped[20] semiconductor nanocomposites, the concept of magnetic photocatalysts shows better charge carrier separation function. Hence, development of photocatalyst possessing ferromagnetic property in tune with visible-light activity has become an important topic in the photocatalysis research today.

In the present work, focus on the structural, electronic, magnetic and photocatalytic properties of Sn-TiO_2 NPs with different Sn doping levels were studied. Using a simple hydrothermal method and various amounts of $SnCl_4$ added into a titanium nitrate aqueous solution, anatase, mixture (anatase-rutile) and rutile phases of Sn-TiO_2 NPs were obtained. In addition, methyl orange (MO) and *R*PhOH (where PhOH is phenol and *R* = 3-NH_2, H and 4-Cl) were chosen as model pollutants to evaluate the photocatalytic activity of Sn-TiO_2 samples under visible and UV light irradiation in water, respectively. Significant relation was observed between the Hammett substitution constant (σ) of *R*PhOH and the photocatalytic degradation efficiency (PDE) of Sn-TiO_2 NPs. It was revealed that structural, electronic, magnetic and photocatalytic properties are closely related to the Sn doping level.

In addition, we emphasize a combined study of photocatalytic and ferromagnetic characters at room temperature on Sn-TiO_2 samples, which is the most emerging field in environmental remediation and in the development of magnetic material. Even after a decade-long research, the actual mechanism of ferromagnetism combined with photocatalytic behavior in these materials is still not understood, although hints about some of the key factors that contribute to the magnetism have been pointed out.[21] It is believed that oxygen vacancy, phase change and doping level play a major role in the RTFM semiconductor oxides.[22] However, demonstration of a direct correlation between the magnetism, dopant concentration, oxygen vacancy and photocatalytic activity has been difficult.[23] Because of these reasons, in this work, we made an effort to investigate the true role of tin ions on the above properties of prepared Sn-TiO_2 NPs.

2. Experimental

2.1. Chemicals

Titanium isopropoxide and $SnCl_4$ in methylene chloride were purchased from Sigma Aldrich. Ammonium hydroxide, hydrogen peroxide, oxalic acid and nitric acid were purchased from Himedia and SD Fine Chemicals (India). SnO_2, TiO_2 (rutile), MO and *R*PhOH were purchased from Aladdin chemicals (China). All the chemicals are at least analytical grade with no further treatment. Ethanol was purified by distillation and de-ionized water was used for solution preparation.

2.2. Instrumentation

Diffuse reflectance spectra (DRS) were obtained for the dry-pressed disk samples using a Shimadzu UV 2450 double-beam spectrophotometer equipped with an integrating sphere (ISR- 2200) assembly using $BaSO_4$ as a reference sample. X-ray diffraction (XRD) patterns were recorded in 2θ range 20-80° with step size 0.02° using CuK_α radiation on an X-Pert PANalytical X-ray diffractometer. The average particle size was calculated by the Scherrer equation from the full width at half maximum of the strongest reflections: (101) for anatase and (110) for rutile. ^{119}Sn Mössbauer spectra were collected on a Topologic 500A system at room temperature. $Ca^{119m}SnO_3$ source was moved in a constant acceleration mode. X-ray photoelectron spectra (XPS) were measured on ESCALAB 250Xi X-ray photoelectron spectrometer with monochromatic source Al K_α and the binding energy (B.E.) was calibrated using contaminated carbon as an internal standard (C 1*s* B.E. 284.6 eV). Steady state fluorescence emission spectra were recorded on Spex FluoroLog-3 spectrofluorometer (Jobin-Yvon Inc.) using 450 W xenon lamp and equipped with a Hamamatsu R928 photomultiplier tube. Time-resolved fluorescence decay measurements were carried out using nano-LED (λ_{exc} = 295 nm) source for excitation with repetition rate 10 kHz. Life times were determined by fitting the data to exponential decay models using software packages of the commercially available DAS6 v6.2-Horiba Jobin Yvon. The goodness of fit was assessed by minimizing the reduced chi-squared function (χ^2). The Raman spectra were recorded on the Jobin Yvon Horibra LABRAMR1100 micro-Raman spectrophotometer. Magnetization measurements were carried out using

vibrating sample magnetometer (VSM) in powder form on Lakeshore-7404 at room temperature. Surface morphology and elemental mapping were examined by scanning electron microscope-energy dispersive X-ray detector (SEM-EDX, Hitachi, S-3400N microscope). Brunauer-Emmett-Teller (BET) surface areas were measured by nitrogen adsorption at -196 ºC using a Micromeritics ASAP 2010 apparatus. The high resolution transmission electron microscope (HRTEM) images were taken on JEOL JEM-2000EX microscope. The spectrophotometric measurements were carried out on a GBC Cintra UV-vis spectrophotometer.

2.3. Preparation of Sn-TiO_2 samples

The preparation process was similar to our previous report[17] but with slight modification. Firstly, 5 mol reddish brown titanium nitrate solution was prepared[17] and then 0.05, 1.5, 2.0, 3.0 and 4.0 mL $SnCl_4$ (1 M in methylene chloride) solutions were separately added into the titanium nitrate solution under magnetic stirring. Furthermore, 100 mL oxalic acid solution (0.6 M) was introduced drop wise to the mixture within 2 h under magnetic stirring to ensure complete precipitation, respectively. The resultant suspension was separately transferred into a Teflon lined stainless steel autoclave, sealed and heated at 110 ºC for 4 h with the pressure maintained at 18 psi. Finally, the precipitates were filtered, washed with distilled water followed by ethanol, and dried in air at 90 ºC for 12 h. The dried precipitates were further calcined at 400 ºC for 4 h in a muffle furnace to get Sn-TiO_2 nanocrystal samples. The undoped TiO_2 sample was synthesized by the same process without

addition of $SnCl_4$ precursor. Hereafter, the Sn doped TiO_2 samples are denoted as Sn-Ti-x (x represents the atom ratio % of Sn/Ti, x = 0-1.37). Sn-Ti-0.12 sample has already reported in our previous paper,[17] however some of the experimental values were taken for comparison purpose.

2.4. Photocatalytic activity

The photocatalytic activities of the samples were evaluated by photodegradation of MO (10^{-5} M) using PE.ILC CERMAX xenon illumination system model LX 175 / 300 attached with CX-04E power supply (10 A) and with a 400 nm long-pass filter was used as the visible light source. Moreover photodegradation of *R*PhOH (10^{-4} M) using a 27 W black light lamp (FPL27BLB, Sankyo Denki, Japan), which emitted light with a wavelength of 368 nm UV light. The distance between the lamp and the solution was 8.0 cm. The intensity of the UV light was adjusted to ~2.6 mW cm^{-2}. All of the experiments were performed in a dark box. In a general photocatalytic experiment, 50 mg catalyst was dispersed in an 80 mL MO or *R*PhOH aqueous solution in a 100 mL glass beaker at room temperature and neutral pH conditions. The suspension was put in dark and magnetically stirred for 45 min to reach the adsorption–desorption equilibrium. Prior to light irradiation, the suspension was continuously stirred by a magnetic stirrer for complete mixing. 3 mL aliquots were periodically taken out from the suspension to centrifuge (15,000 rpm, 2 min) at the interval of 60 min during the evaluation process. The supernatants were measured by the GBC Cintra instrument to record the changes of absorption values at the various

wavelengths such as 464, 269, 282 and 279 nm relative to the initial MO, PhOH, 3-NH_2PhOH and 4-ClPhOH aqueous solutions, respectively. The photodegradation efficiency (PDE) was calculated via the formula PDE = $(A_0 - A_t/A_0) \times 100\%$, where A_0 is the absorbance of initial MO or *R*PhOH solution and A_t is the absorbance of MO or *R*PhOH solution measured at various irradiation time at corresponding wavelengths. In typical ferromagnetic test, the Sn-Ti-0.05 catalyst was isolated from phenol degraded aqueous solution under UV light irradiation at 300 min using centrifuge and washed thoroughly with deionized water and dried at room temperature.

3. Results and discussion

3.1. Structural and morphological properties

The XRD patterns of Sn-Ti-x (x = 0, 0.05 and 0.12) samples, as shown in Fig. 1, diffraction peaks observed at 2θ = 25.3, 36.9, 37.7, 38.5, 48, 51.9, 53.8, 55.1, 62.6, 68.7, and 75º reveal the existence of predominant anatase phase, however, in the case of other Sn-Ti-x (x = 0.17, 0.30, 1.14 and 1.37) samples peaks observed at 2θ = 27.4, 39, 41, and 44º are referred for the rutile phase.[7] These results indicate that with increasing tin atomic ratio, the crystalline phase of the as prepared Sn-TiO_2 samples consist some impurity phase such as rutile, which was confirmed from Fig. 1. The diffraction patterns of Sn-Ti-x (x = 1.14 and 1.37) samples contain two additional peaks at 2θ = 27.2 and 34.4º that are ascribed to SnO_2 with rutile (casseterite tetragonal) structure, indicating SnO_2 has coupled with TiO_2 rutile particles in two of the samples with increase in tin content.[24]

Fig. 1b and c clearly show that the peak intensities of anatase Sn-Ti-x samples decreased and rutile peak intensities increased with the increase of tin content. The rutile (110) reflection appears at ~27°, which is intermediate to that of the pure TiO_2 (27.4°, 2θ) and pure SnO_2 (26.6°, 2θ) positions.[25] It can also be ascribed that some of the lattice constants in rutile, SnO_2 and TiO_2 were observed, in addition, lattice distortion was induced by the substitution of Sn for Ti.[26] Average particle sizes were estimated from the XRD patterns using the Scherrer equation from 25 and 27° reflections (Table 1).[27] In the case of anatase phases, the crystalline size of Sn-Ti-x (x = 0, 0.05 and 0.12) samples are bigger than that of rutile Sn-Ti-1.37 samples. According to the previous report, a critical particle size should be required for the crystalline phase transformation from anatase to rutile, thus the rutile size should be smaller than anatase one in the coexistence of anatase and rutile phases of TiO_2.[28,29]

The crystalline phase analysis of the Sn-Ti-x samples obtained in this work was further investigated by Raman spectroscopy as shown in Fig. 2. Predominant anatase peaks were observed appearing at 144, 399, 521 and 638 cm^{-1} in Sn-Ti-x (x = 0, 0.05 and 0.12) samples. The Raman peak intensities of anatase Sn-Ti-x samples decreased with the increase of tin content. With further increase in Sn content, four strong peaks were observed at 149, 402, 522 and 638 cm^{-1}, which are similar to that of anatase TiO_2,[30] moreover, one additional weak rutile peak is observed at 433 cm^{-1} in Sn-Ti-0.17 and Sn-Ti-0.30. In the high Sn content samples, three strong peaks were observed at 262, 436, and 618 cm^{-1}, which are quite different to those of pure rutile TiO_2 (235, 446 and 611 cm^{-1}) and can be explained due to SnO_2 peaks in coexistence

with rutile TiO_2 phase. Additional formation of SnO_2 crystalline phase was observed at ~776 and ~448 cm^{-1}, which indicate that some amount of tin exists as tin oxide crystalline phase coupled with rutile TiO_2 in Sn-Ti-1.14 and Sn-Ti-1.37 samples.[31] Therefore, the results of Raman spectra of the samples confirm the results of XRD patterns.

Fig. 3 presents the ^{119}Sn Mössbauer spectra of the Sn-Ti-x samples at room temperature. A summary of the obtained ^{119}Sn Mössbauer parameters are given in Table 2. The isomer shift (*IS*) values of all components indicated that all tin atoms in all prepared samples were tetravalent (Sn^{4+}). The absence of absorption peaks in the Doppler velocity range of 2-4 mms^{-1} indicates Sn^{2+} ion free in the Sn-Ti-x samples.[32] The difference in the quadrupole splitting (*QS*) values of the component peaks implied that Sn atoms existed under different asymmetry of coordination polyhedron around Sn atoms in the TiO_2 lattice. The spectra of low level Sn doped samples of Sn-Ti-x (x = 0.05, 0.12 and 0.17) were fitted by one doublet, respectively. The obtained *IS* values are very close to that of typical Sn^{4+} bonded to oxygen in octahedral environments.[33] More precisely, *IS* are found to be positive (*IS* = 0.10-0.14 mms^{-1} and *QS* = 1.02-1.30 mms^{-1}), which are consistent with the values reported for the Sn^{4+} dopant in transition metal oxides.[34,35] This fact thus suggests the occurrence of Ti–O–Sn–O–Ti chain fragments in the lattice and consequently insertion of dopant into the matrix.[36] The spectra of high level Sn doped samples of Sn-Ti-x (x = 0.30, 1.14 and 1.37) were decomposed into two doublets, both of these with unusually high *QS* were assigned to the defects playing very important role in the realization of

ferromagnetism in these materials. The parameters of doublet D1 correspond well to those characteristics of Sn doped TiO_2 with lattice crystal defects (*IS* = 0.11-0.14 mms^{-1} and *QS* = 1.34-1.76 mms^{-1}), while doublet D2 (*IS* = 0.09-0.16 mms^{-1} and *QS* = 4.28-5.86 mms^{-1}) can be associated with a much distorted Sn microenvironment due to a neighboring crystal defect like a vacancy.[37] The spectra show that defects occur in a very high amount in these simple hydrothermal prepared tin doped titania samples. The doublets having very large *QS* are associated with defects, vacancies, stabilized by doping of Sn^{4+} in TiO_2 system. Considering the unusual large *QS* and line width (*LW*) values, it is also possible to result in magnetic interaction. From XRD results small amount of the SnO_2 coupled with TiO_2, this may also possible to exist large *QS* and *LW* values. Anyway, the ^{119}Sn Mössbauer spectral results clearly showed the existence of structural defects, which have an essential role in the appearance of ferromagnetism.

XPS analysis was performed to further study the chemical state of tin in TiO_2 matrix. Fig. 4 shows the survey, Ti 2*p*, Sn 3*d* and O 1*s* XPS spectra of a typical Sn-Ti-0.17 sample. It can be seen that XPS peak positions of Ti $2p_{3/2}$ and Ti $2p_{1/2}$ located at 458.4 and 464.3 eV, indicate that Ti element mainly exist in the chemical state of Ti^{4+}. The peak was observed with the B.E. of 529.6 eV corresponds to oxygen in TiO_2 lattice (O_L). The doublet peaks observed at 486.1 and 494.6 eV in the Sn 3d XPS spectrum are ascribed to Sn $3d_{5/2}$ and Sn $3d_{3/2}$ of the substituted Sn^{4+} ion as dopants in the TiO_2 lattice, since the peak position of Sn $3d_{5/2}$ (486.1 eV) was located between that of SnO_2 (486.6 eV) and metallic Sn (484.4 eV).[38] The XPS analysis

infers that the Sn^{4+} ion can conveniently replace Ti^{4+} ion in the lattice and enter the lattice of TiO_2 as explored by ^{119}Sn Mössbauer spectroscopy.

SEM analysis was employed to understand the surface morphology of Sn-Ti-x crystals. Fig. S1 depicts SEM images, which illustrate that the particles mainly belong to anatase and anatase-rutile mixed phases, loosely agglomerated, spherical with nanosized particles, and significantly good in crystalline quality. The compositions of the Sn-Ti-x samples were analyzed by EDX as shown in Figs. S2-S5. The atomic percentages of Ti, Sn and O elements obtained by EDX analysis are presented in Table 3. The distribution of Ti, O and Sn elements in a typical Sn-Ti-0.05 sample could be seen on the elemental mapping and line spectrum, where the relative location of each constituent can be spotted in different colors as shown in Fig. 5. Although this percentage of Sn/Ti has approached upto the detection limit of EDX and some background noise have kicked in, we can find that Sn atoms have been incorporated over the entire TiO_2 NPs obviously as in Fig. 5d. The EDX elemental maps and line scan spectra confirmed the uniform distribution of O, Ti, and Sn species in lattice of nanosized Sn-Ti-x samples.

Fig. S6 shows the N_2 adsorption-desorption isotherms and Barret-Joyner-Halenda (BJH) pore size distribution curves of Sn-Ti-x samples with a significant hysteresis loop observed in the relative pressure (p/p_0) range of 0.95-0.99. This property implies the presence of mesopores. This result is further confirmed by the pore size distribution curve which indicates the predominance of pores 5.34-13.21 nm in diameter. The BET and Langmuir surface area results are presented in Table 3,

respectively.

Fig. 6 shows the TEM images of typical Sn-Ti-0.05, Sn-Ti-0.30 and Sn-Ti-1.37 samples. NPs with a diameter of 5-10 nm were observed in all as prepared samples. The electron diffraction patterns of the selected area on anatase Sn-Ti-0.05 sample (inset Fig. 6a) showed the strong Debye-Scherrer rings and additionally complicated bright spots were observed for Sn-Ti-0.30 and Sn-Ti-1.37 samples (inset Fig. 6b,c), indicating the coexistence of anatase-rutile or rutile-casseterite crystalline phases.[39]

Fig. 7 displays the HRTEM images of Sn-Ti-0.05, Sn-Ti-0.30 and Sn-Ti-1.37 samples. For the pure anatase structure, the fringe spacing (*d*) of (101) crystallographic plane was determined to be 3.52 Å,[9] while Sn^{4+} doped TiO_2 samples, it was determined to fall in the range 3.52 to 3.55 Å. This implies that Sn^{4+} ions were doped in the TiO_2 lattice in substitutional mode, since the ionic radius of Sn^{4+} (0.69 Å) is larger than that of the lattice Ti^{4+} (0.53 Å).[40] Furthermore, a fringe spacing of ~3.22 Å corresponds to the (110) plane of rutile TiO_2 phase was observed for Sn-Ti-0.30 crystals. The crystallographic planes of SnO_2 cassiterite (101) fringe spacing observed at 2.64 Å, further confirmed that SnO_2 was coupled with TiO_2 in Sn-Ti-1.37 sample. The structural, chemical and morphological characterizations performed using XRD, XPS, Raman, ^{119}Sn Mössbauer spectroscopy, SEM-EDX and HRTEM clearly explored the octahedral substitution of Sn^{4+} for Ti^{4+} in the Ti-Sn-x (x = 0.5, 0.12 and 0.17) crystal lattice, in addition SnO_2 was coupled with TiO_2 in remaining Ti-Sn-x (x = 0.30, 1.14 and 1.37) samples.

3.2. Structurally assisted photocatalytic activity

In order to confirm the visible-light-induced photocatalysis, the MO degradation was carried out by a CERMAX xenon illumination system attached with a light filter 400 nm cut-off wavelength. A typical adsorption process was performed in the same reaction conditions before light irradiation as presented in Fig. S7. Sn-Ti-0.05 and Sn-Ti-0.12 samples exhibited little higher adsorption capacity due to their large surface areas and pore sizes, which are beneficial for the improvement of photocatalytic activity.

Fig. 8a shows the repetitive scan spectra of photodegradation of MO with the Sn-Ti-x samples suspended in water. It is observed that a gradual decrease in the absorption bands at 268 and 464 nm of MO with the increase of the irradiation time.[41] In Fig. 8b, the PDE of MO is plotted as a function of reaction time which indicates that the PDE of Sn-Ti-x samples can be improved by doping an appropriate density of Sn^{4+} dopant. The Sn-Ti-x samples with x = 0.05 and 0.12 exhibited higher photocatalytic activity. However, if x increases steadily, the photocatalytic activity begins to fall down appropriately. This behavior is due to the phase transformation of the crystals as the dopant content is enhanced. In general, the photocatalytic performance of anatase is considered superior to that of the more stable rutile phase of titania. Some of the earlier reports[42,43] attributed that anatase is very effective in photocatalytic activity due to higher density of localized states, the existence of surface-adsorbed hydroxyl species and slower charge carrier recombination in the crystals.

The UV-light-induced photocatalysis was confirmed by the degradation of *R*PhOH as shown in Fig. 9. In Fig. 10a, the PDE of phenol is plotted as a function of reaction time. There was low observable degradation of phenol over the undoped anatase, rutile TiO_2 and SnO_2 samples. However, in the presence of Sn-Ti-x (x = 0.05, 0.12 and 0.17) a rapid degradation of phenol occurred by UV light irradiation. Phenol was removed upto ~70% on 240 min irradiation using Sn-Ti-x catalyst. It can be concluded that the tin doping into the anatase phase of TiO_2 is efficient for the photocatalytic degradation of the sample under study.

It is known that the properties of phenolic compounds can be drastically affected by the electronic nature of *R* group substituents. In the present work, substituent effect of R group on the photocatalytic activity over Sn-Ti-0.05 sample was studied using *R*PhOH (*R* = H, 3-NH_2 and 4-Cl). The Hammett's substitution constant (σ) was used to establish a relation between the PDE with the substituted phenols as shown in Fig. 10b. These were defined from the ionization constants of the appropriately substituted benzene derivatives such as benzoic acid, phenol, aniline etc., as $\sigma(X) = \log K_X - \log K_H$, where K_H is the ionization constant for benzene derivative in water at 25 °C and K_X is the corresponding constant for a *meta*- (σ_m) or a *para* substituted (σ_p) benzene derivatives. The PDE was found to be dependent on the electron donating / withdrawing effect of the substituent *R* group on the aromatic ring of *R*PhOH. The results indicate that the highest PDE was observed for 3-NH_2PhOH (σ = -0.16) and lowest for 4-ClPhOH (σ = 0.23) due to electrophilic nature of organic substrates of phenolic compounds.

3.3. Optically and luminescently dependent photocatalytic activity

Fig. S8 shows the UV-vis DRS of the Sn-Ti-x samples. The band gap can be estimated from the Kubelka-Munk curve as shown in Fig. S9 and listed in Table 1. It can be seen that Sn-Ti-0.05 exhibits a slight red shift as compared to Sn-Ti-0, the band gap energy decreased from 3.30 to 3.18 eV, which might result from doping effects.[44,45] Rutile Sn-Ti-1.37 exhibits a slight blue shift as compared to anatase Sn-Ti-0.05, and the band gap energy increased from 3.18 to 3.24 eV, such an enhancement in BGE is expected to improve the photocatalytic performance of anatase Sn-Ti-x samples. Anatase Sn-Ti-0 sample could absorb mainly the UV light with wavelength below 400 nm due to its intrinsic band gap energy (anatase TiO_2 = 3.30 eV). However, compared with the undoped TiO_2, the absorption edge thresholds of the Sn-Ti-x (x = 0.05 and 0.12) samples were distinctly shifted towards the visible region (Fig. S8). Therefore efficiencies of the doped anatase Sn-Ti-x (x = 0.05 and 0.12) photocatalysts are higher under visible light irradiation, revealing a positive effect of the presence of tin and presumably structural defects or oxygen vacancies. It can be concluded that the tin doping of the anatase phase of TiO_2 is beneficial for the photocatalytic activity in the present study. This interpretation can also be supported by the facts that the decrease of anatase phase proportion from Sn-Ti-0.05 to Sn-Ti-1.37 leads to lower phenol photo degradation efficiencies under UV irradiation (Fig. 10). Moreover, oxygen vacancies and structural defects also influence the photocatalytic activities.[46]

Information regarding the presence of surface states, formation of photoinduced charge carriers, and their recombination kinetics can be drawn from the photoluminescence (PL) spectra of semiconductor materials.[47] PL spectra of Sn-Ti-x samples with excitations at 330 nm are presented in Fig. 11. Broad emission in the spectral range from 350 to 600 nm was observed as well as well-resolved peaks / shoulders at 410, 417, 438, 449, 466, 480, 490 and 560 nm corresponding energy of 3.03, 2.98, 2.83, 2.76, 2.66, 2.59, 2.53 and 2.22 eV, respectively were seen. A change in Sn^{4+} dopant density in TiO_2 altered the intensity and or change the shape and peak position of the PL spectra compared to spectrum of predominantly anatase Sn-Ti-x (0 and 0.05) samples. It was found that the steady state emission spectrum contains a narrower UV emission located near 390 nm (3.18 eV) and a broader emission range from 450 to 491 nm.[48] A strong green emission was observed at 560 nm (2.22 eV) as shown Fig. 11. Therefore, emissions likely originated from surface defects, such as ionizable oxygen vacancies and the recombination of self-trapped excitons (STEs) which are localized within TiO_6 octahedra.[49] The formation of oxygen vacancies were confirmed from EPR measurement for Sn-Ti-0.12 sample in our previous study.[17] The STEs in the present samples were originated from band-to-band excitation where the excited electron and hole created a local deformation of TiO_6 octahedra and thus localized themselves into surface defect states of TiO_2. Two peaks around 480 and 560 nm were observed for Sn-Ti-x samples (Fig. 11), which are attributed to the transition from oxygen vacancies with two-trapped electrons and one-trapped electron in the valence band of Sn-Ti-x samples, respectively. The energy levels relate to these

two types of oxygen vacancies were located at 0.51 eV and 0.87 eV below the conduction band of Sn-Ti-x NPs, respectively,[50] which implies that the recombination of charge carriers were effectively suppressed upon Sn-Ti-x samples.

Similar PL spectra were reported by Serpone et al.[51] and Chetri et al.[52] PL intensities resulting from efficient charge separation was already reported for TiO_2 and ZnO doped with Sn, W, Ag, and Au.[53,54] These semiconductors showing lower PL intensities were also reported to exhibit higher photocatalytic activity.[55] The defect concentrations and life times of photoexcited species plays an important role in photocatalysis, investigation of photocatalysts through PL spectroscopy is important to obtain critical reasons behind the enhanced photocatalytic activity. A strong correlation between PL intensities and photocatalytic activities were established by previous researches.[47,53] PL emission results from the recombination of photoinduced charge carriers, the stronger the PL signal, the higher the recombination rate of the photoinduced charge carriers.[56] When the recombination rate decreases, more photoinduced charge carriers can participate in dye photodegradation, resulting in the enhancement of photocatalytic activity.[57] Anatase Sn-Ti-0.05 sample, which are less luminescent with decreased intensity than rutile Sn-Ti-1.37, has a wider band gap resulting in efficient electron-hole separation. The reduction in PL intensity can also be caused by an increase in non-radiative or radiative recombination at longer wavelengths outside the recorded PL range. These effects are occurring in nanocomposite system as a consequence of charge trapping on surfaces or the inter phases between the two oxide phases.[52]

The defects in Sn-Ti-x samples were further characterized by lifetime measurements. The PL lifetime decay profiles of Sn-Ti-x samples with different dopant concentrations are shown in Fig. S10 and PL lifetime parameters are presented in Table 1. The decay follows tri-exponential kinetics. The photoinduced charge carriers relax to the shallow-trap levels, radiantly recombine with the lifetime of τ_1. The component of shorter lifetime (τ_1) was caused by the free annihilation of positrons in defect-free crystal. In a disordered system, small vacancies or shallow positron traps can reduce the surrounding electron density and thus increase the lifetime of τ_1.[58] The τ_1 values for Sn-Ti-x are from 2.39 to 2.88 ns, longer than that of undoped Sn-Ti-0 (1.48 ns), indicating the existence of monovacancies or point defects in TiO_2.[59,60] The photoinduced charge carriers could be relaxed to the deep-trap levels related to the oxygen vacancies of the nanostructure and consequently recombine radiantly with a much longer lifetime of τ_2, which was also increased from undoped TiO_2 to Sn doped TiO_2. The fast component with lifetime τ_3 may be due to this near band edge relaxation of TiO_2. The lifetime becomes longer due to a lack of significant overlap between electron and hole wave functions.

From Table 1, the values of τ_3 decrease from undoped to Sn doped TiO_2 samples, whereas the values of τ_1 and τ_2 corresponding to the defect-related emissions decrease in the opposite order. Thus, the lattice defects and oxygen vacancies are more pronounced in the Sn doped TiO_2 samples than that of undoped sample. Consequently, it may be concluded that the Sn doping might increase the concentrations of photoinduced charge carriers in the different trap levels and oxygen vacancies, which

implies the longer lifetime of the doped nanostructure than the undoped one.[61] Among all samples, longer PL lifetime observed for Sn-Ti-0.05 and Sn-Ti-0.12 samples indicates lower recombination rate of the electron-hole pairs and more efficient photocatalytic performance.[62]

3.4. Ferromagnetically assisted photocatalytic activity

The field dependence of magnetizations for Sn-Ti-x samples was measured at room temperature as shown in Fig. 12. Related saturation magnetization (M_s), coercivity (H_c) and remanence (M_r) of all the samples are listed in Table 2. Significant hysteresis loops in the M−H curves indicated the weak RTFM behavior (Fig. 12a) of anatase Sn-Ti-x (x = 0, 0.05 and 0.12) and ferromagnetic with diamagnetic behaviors for these remained samples (Fig. 12b).[63] The M_s values increased from 10.3 to 129.6 memu g^{-1} with increasing x from 0 to 0.12, it could be due to spin reorientation arising from spin–spin interaction between Sn–O and Ti–O dipoles.[16] This implies that the interface has an additional effect on magnetism. There can be a large amount of lattice mismatch at the interface in Sn-Ti-x samples with a high possibility of presence of uncompensated bonds of Sn, Ti and O. The ferromagnetic interaction in TiO_2 is weaker than SnO_2; hence the spins at the interface layer come across two different kind of interaction. Ferromagnetic interaction of SnO_2 might extend the interaction in TiO_2 via Ti vacancies and hence increase M_r. This extension of ferromagnetic interaction should also be the reason of enhanced M_s in Sn-Ti-x samples. The pristine SnO_2 sample reported the diamagnetic behavior[64,65] with the very weak ferromagnetic

signal resulting possibly from native defects,[66,67] while the Sn-Ti-x (x = 0.17, 0.30, 1.14 and 1.37) displays the mixture of diamagnetic and ferromagnetic behaviors as shown in Fig. 12b. It can be concluded that the observed magnetic properties are significant and the ferromagnetic and diamagnetic signals are due to the incorporation of Sn^{4+} ions in TiO_2 host matrix. Therefore, when the magnetic moments are very weak for Sn-Ti-x samples, the intrinsic diamagnetic back ground of SnO_2 takes dominant status again.

Considering the relation between magnetic and photocatalytic activities of Sn-Ti-x NPs, the anatase RTFM Sn-Ti-x (0.05 and 0.12) NPs showed high photocatalytic activity (Table 3). RTFM observed in these undoped and Sn doped TiO_2 NPs can be attributed to oxygen vacancies and/or defects. Doping these NPs with low concentrations of Sn^{4+} ions increased both photocatalytic activity and ferromagnetism, presumably due to the creation of additional oxygen or titanium vacancies. However, when Sn doping concentration x increased above 0.12, while both photocatalytic activity and magnetic moment of Sn-Ti-x NPs rapidly decreased. Since the decrease in PDE could be attributed to the high rate of e^--h^+ recombination facilitated by the doped Sn^{4+} ions and due to formation of diamagnetic rutile phases, we tentatively assign the reduction in M_s also to the reduction of charge carriers. High electron-hole concentration is necessary for both interfacial electron transfer models in photocatalytic process as well as the charge-transfer ferromagnetism to work. The experimental results show that the magnetic property of Sn-Ti-x were caused by the double exchange between Sn^{4+} and Ti^{4+} as well as the defective state in them, the

Sn-Ti-0.05 and Sn-Ti-0.12 samples show higher ferromagnetic and photocatalytic properties than that of other Sn-Ti-x (x = 0.17, 0.30, 1.14 and 1.37) samples because of its higher defective states or oxygen vacancies and stronger visible light absorption.

To make sure that the RTFM was related to the presence of oxygen vacancies in the Sn-Ti-x samples, PL measurements are correlated with magnetic and photocatalytic results for the samples. To correlate the presence of RTFM, PL spectra and photocatalytic activity studies of the Sn-Ti-x (x = 0.05, 0.17, 0.30, 1.14 and 1.37) samples, the observed M_r, PDE values and intensity of the emission band have been plotted with Sn doping level and shown in Fig. 13. The result suggests that the doping level and oxygen vacancies in the Sn-Ti-x nanocrystals are mainly responsible for RTFM, photocatalytic activity and intensity variation of PL emission band of Sn-Ti-x samples. It has been shown that low levels of Sn doping in TiO_2 can strongly reduce the energy for oxygen vacancy formation, resulting in increasing number of oxygen vacancies.[68] This will reduce e^--h^+ recombination rate and result in the higher PDE and alternatively high level of oxygen vacancies[69] makes strong ferromagnetic behavior in metal oxide semiconductor NPs. The decrease in the value of M_r can be attributed to the decrease in the density of oxygen vacancies at higher Sn doping level. The decrease in the density of oxygen vacancies at higher Sn doping level was also confirmed by PL spectroscopic results. Oxygen vacancies are found to be the main cause for enhanced photocatalytic activity of metal oxide nanostructures.[23] Contrast behavior was observed for Sn-Ti-0.17 sample, low M_r value and high PDE observed

was due to predominant synergetic effect between anatase-rutile mixed phases[70] than oxygen vacancies or magnetic nature. These new weak ferromagnetic Sn-Ti-0.05 and Sn-Ti-0.12 samples were extremely effective for the MO and *R*PhOH degradation, and maintained relatively high activity. In addition, we investigate the combined photocatalyst and ferromagnetic character at room temperature in the Sn-Ti-x NPs, which has the potential to collect the powders during waste water treatment. The room temperature hysteresis loops of Sn-Ti-0.05 sample before and after isolated from waste water treatment were measured to clarify the role of photocatalyst to make strong ferromagnetic character (Fig. S11). The ferromagnetic character is somewhat higher for typical waste water treated Sn-Ti-0.05 photocatalyst under UV light irradiation (M_s = 21.66 memu g^{-1} , H_c = 117.04 G and M_r = 2.07 memu g^{-1}) instead of untreated samples (M_s = 16.66 memu g^{-1}, H_c = 105.33 G and M_r = 1.30 memu g^{-1}). This is due to creation of more oxygen vacancies on the UV illuminated Sn-Ti-x samples,[71] but further investigations are needed to determine creation of ferromagnetism due to waste water treated photocatalysts. Hence the RTFM should be extended to various potential applications, such as spintronics, photodegradation, catalysis, separation, and purification processes.

5. Conclusions

Tin doped TiO_2 NPs were successfully synthesized by simple hydrothermal method. Various spectroscopic measurements indicated that the presence of structural, optical, magnetic effects and oxygen vacancies in the Sn-Ti-x system. The

photocatalytic properties of Sn-Ti-x samples were tested, and the results showed that small amount of tin doped TiO_2 which preferably formed anatase phase with oxygen vacancies had the improved photocatalytic activity due to the more efficient separation of photoinduced electrons and holes on its surface. The major effects of Sn doping are considered to: (i) the formation of Sn-doped anatase phase, two phase (anatase and rutile) coexist and rutile phase with $x < 0.12$, $0.12 < x < 0.30$ and $x \geq 1.14$, respectively, (ii) the enhanced light absorption property in the UV and visible region and shift of absorption edge, (iii) Sn content in TiO_2 assisted ferromagnetic to ferromagnetic with diamagnetic characters and (iv) the photocatalytic activities showed structural, luminescent and ferromagnetic dependences. This study could point out a potential way to develop new and more active RTFM tin doped titania photocatalysts for the waste water treatment.

Acknowledgements

Prof. J. Wang is grateful to National Natural Science Foundation of China (No. 21476232). Prof. KA is thankful to CSIR, New Delhi (No. 01 (2570)/12/EMR-II/3.4.2012) for financial support through a major research project.

References

1 L. Sun, W. Wu, S. Yang, J. Zhou, M. Hong, X. Xiao, F. Ren and C. Jiang, *ACS Appl. Mater. Interfaces*, 2014, **6**, 1113–1124.

2 K. Anbalagan, A. S. Ganeshraja and C. M. Mahalakshmi, *Mater. Chem. Phys*., 2012,

134, 747–754.

3 K. Anbalagan and L. D. Stephen, *Transit. Met. Chem*., 2009, **34**, 915–923.

4 M. Dahl, Y. Liu and Y. Yin, *Chem. Rev*., 2014, **114**, 9853–9889.

5 F. Yu, Y. Wang, H. Tang, C. Jin, X. Liu and J. Wang, *Catal. Commun*., 2014, **51**, 46–52.

6 X. Li, J. Wang, A. I. Rykov, V. K. Sharma, H. Wei, C. Jin, X. Liu, M. Li, S. Yu, C. Sun and D. D. Dionysiou, *Catal. Sci. Technol*., 2015, **5**, 504–514.

7 M. F. Abdel-Messih, M. A. Ahmed and A. S. El-Sayed, *J. Photochem. Photobiol. A: Chem*., 2013, **260**, 1–8.

8 H. A. J .L. Mourao, W. A. Junior and C. Ribeiro, *Mater. Chem. Phys*., 2012, **135**, 524–532.

9 Y. Cao, T. He, L. Zhao, E. Wang, W. Yang and Y. Cao, *J. Phys. Chem*. C, 2009, **113**, 18121–18124.

10 Y. Wang, Y. Zhang, F. Yu, C. Jin, X. Liu, J. Ma,Y. Wang, Y. Huang and J. Wang, *Catal. Today*, 2015, **258**, 112–119.

11 S. Phokha, S. Pinitsoontorn and S. Maensiri, *Nano-Micro Lett*., 2013, **5**, 223–233.

12 A. Lu, E. L. Salabas and F. Schuth, *Angew. Chem. Int. Ed*., 2007, **46**, 1222−1244.

13 S. Wang, L. Pan, J. Song, W. Mi, J. Zou, L. Wang and X. Zhang, *J. Am. Chem. Soc*., 2015, **137**, 2975−2983.

14 K. Anbalagan, *J. Phys. Chem. C*, 2011, **115**, 3821−3832.

15 A. S. Ganeshraja, Investigation of Ferromagnetism in Nano-TiO_2 Containing Transition Metal Ion Impurity Produced by Photoreduction Process (Ph.D. thesis),

Pondicherry University, 2013.

16 P. Chetri, P. Basyach and A. Choudhury, *J. Solid State Chem*. 2014, **220**, 124−131.

17 A. S. Ganeshraja, A. S. Clara, K. Rajkumar, Y. Wang, Y. Wang, J. Wang and K. Anbalagan, *Appl. Surf. Sci*., 2015, **353**, 553–563.

18 C. Cheng, A. Amini, C. Zhu, Z. Xu, H. Song and N. Wang, *Sci. Rep*., 2014, **4**, 4181, DOI:10.1038/srep04181.

19 A. Charanpahari, S. G. Ghugal, S. S. Umare and R. Sasikala, *New J. Chem*., 2015, **39**, 3629–3638.

20 N. C. Khang, N. V. Khanh, N. H. Anh, D. T. Nga and N. V. Minh, *Adv. Nat. Sci*.: *Nanosci. Nanotechnol*., 2011, **2**, 015008-1–4.

21 K. Dodge, J. Chess, J. Eixenberger, G. Alanko, C.B. Hanna and A. Punnoose, *J. Appl. Phys*., 2013, **113**, 17B504-1–3.

22 A. Sundaresan and C. N. R. Rao, *Nano Today*, 2009, **4,** 96–106.

23 S. Kumar, A. K. Ojha, *J. Alloys Compd*. 2015, **644**, 654–662.

24 A. Bouaine, N. Brihi, G. Schmerber, C. Ulhaq-Bouillet, S. Colis and A. Dinia, *J. Phys. Chem*. C, 2007, **111**, 2924–2928.

25 L. Trotochaud and S. W. Boettcher, *Chem. Mater*., 2011, **23**, 4920–4930.

26 F. Fresno, M. D. Hernandez-Alonso, D. Tudela, J. M. Coronado and J. Soria, *Appl. Catal. B: Environ*., 2008, **84**, 598–606.

27 S. Obregon, M. J. Munoz-Batista, M. Fernandez-Garcia, A. Kubacka and G. Colon, *Appl. Catal. B: Environ*., 2015, **179**, 468–478.

28 K. Sabyrov, N. D. Burrows and R. L. Penn, *Chem. Mater*., 2013, **25**, 1408–1415.

29 F. Yu, J. Wang, K. Zhao, J. Yin, C. Jin and X. Liu, *Chin. J. Catal*., 2013, **34**, 1216–1223.

30 R. Zheng, L. Lin, J. Xie, Y. Zhu and Y. Xie, *J. Phys. Chem. C*, 2008, **112**, 15502–15509.

31 M. M. Oliveira, D. C. Schnitzler and A. J. G. Zarbin, *Chem. Mater*., 2003, **15**, 1903–1909.

32 H. Masaia, T. Miyazaki, K. Mibu, Y. Takahashi and T. Fujiwara, *J. Eur. Ceram. Soc*., 2015, **35**, 2139–2144.

33 N. A. Kyerematenga, F. Vacandio, M.-T. Sougrati, H. Martinez, J.-C. Jumas, P. Knauth and T. Djenizian, *J. Power Sources*, 2013, **224**, 269–277.

34 C. Wang, C. Shao, X. Zhang and Y. Liu, *Inorg. Chem*., 2009, **48**, 7261–7268.

35 P. B. Fabritchnyi, M. V. Korolenko, M. I. Afanasov, M. Danot and E. Janod, *Solid State Commun*., 2003, **125**, 341–346.

36 P. B. Fabritchnyi, E. V. Lamykin, A. M. Babeshkin and A. N. Nesmeyanov, *Solid State Commun*., 1972, **11**, 343–348.

37. K. Nomura, E. Kuzmann, C. A. Barrero, S. Stichleutner and Z. Homonnay, *Hyperfine Interact*, 2008, **184**, 57–62.

38 J. Liu, Y. Zhao, L. Shi, S. Yuan, J. Fang, Z. Wang and M. Zhang, *ACS Appl. Mater. Interfaces*, 2011, **3**, 1261–1268.

39 J. Chang, M. Vithal, I. C. Baek and S. I. Seok, *J. Solid State Chem*., 2009, **182**, 749–756.

40 Y. Cao, W. Yang, W. Zhang, G. Liu and P. Yue, *New. J. Chem*., 2004, **28**, 218–222.

41 A. I. Martinez, D. R. Acosta and G. Cedillo, *Thin Solid Films*, 2005, **490**, 118–123.

42 D. A. H. Hanaor and C. C. Sorrell, *J. Mater. Sci*., 2011, **46**, 855–874.

43 Y. Zhao, J. Liu, L. Shi, S. Yuan, J. Fang, Z. Wang and M. Zhang, *Appl. Catal. B: Environ*., 2010, **100**, 68–76.

44 J. Liu, W. Qin, S. Zuo, Y. Yu and Z. Hao, *J. Hazard. Mater*., 2009, **163**, 273–278.

45 J. Wang, Z. Chen, Y. Liu, C. H. Shek, C. M. L. Wu and J. K. L. Lai, *Sol. Energy Mater. Sol. Cells*, 2014, **128**, 254–259.

46 Y. Zhao, J. Liu, L. Shi, S. Yuan, J. Fang, Z. Wang and M. Zhang, *Appl. Catal. B: Environ*., 2011, **103**, 436–443.

47 L. Jing, Y. Qu, B. Wang, S. Li, B. Jiang, L. Yang, W. Fu, H. Fu and J. Song, *Sol. Energy Mater. Sol. Cells*, 2006, **90**, 1773–1787.

48 T. Tachikawa, J. R. Choi, M. Fujitsuka and T. Majima, *J. Phys. Chem*. *C*, 2008, **112**, 14090–14101.

49 M. Watanabe and T. Hayashi, *J. Lumin*., 2005, **112**, 88–91.

50 A. B. Djurisic, W. C. H. Choy, V. A. L. Roy, Y. H. Leung, C. Y. Kwong, K. W. Cheah, T. K. G. Rao, W. K. Chan, H. F. Lui and C. Surya, *Adv. Funct. Mater*., 2004, **14**, 856–864.

51 N. Serpone, D. Lawless and R. Khairutdinov, *J. Phys. Chem*., 1995, **99**, 16646–16654.

52 P. Chetri, P. Basyach and A. Choudhury, *Chem. Phys*., 2014, **434**, 1–10.

53 R. Georgekutty, M. K. Seery and S. C. Pillai, *J. Phys. Chem. C*, 2008, **112**, 13563–13570.

54 B. Xin, L. Jing, Z. Ren, B. Wang and H. Fu, *J. Phys. Chem. B*, 2005, **109**, 2805–2809.

55 V. Etacheri, M. K. Seery, S. J. Hinder and S. C. Pillai, *Chem. Mater*. 2010, **22**, 3843–3853.

56 M. Yang, C. Hume, S. Lee, Y. Son and J. Lee, *J. Phys. Chem. C*, 2010, **114**, 15292–15297.

57 Y. Li, D. Xu, J. Oh, W. Shen, X. Li and Y. Yu, *ACS Catal*., 2012, **2**, 391–398.

58 X. Jiang, Y. Zhang, J. Jiang, Y. Rong, Y. Wang, Y. Wu and C. Pan, *J. Phys. Chem. C*, 2012, **116**, 22619−22624.

59 H. Murakami, N. Onizuka, J. Sasaki and N. Thonghai, *J. Mater. Sci*., 1998, **33**, 5811−5814.

60 J. Yan, G. Wu, N. Guan, L. Li, Z. Li and X. Cao, *Phys. Chem. Chem. Phys*., 2013, **15**, 10978−10988.

61 K. Das, S. N. Sharma, M. Kumar and S. K. De, *J. Phys. Chem. C*, 2009, **113**, 14783–14792.

62 B. Liu and L. Peng, *J. Alloys Compd*., 2013, **571**, 145−152.

63 Y. Ren, H. Wu, M. Lu, Y. Chen, C. Zhu, P. Gao, M. Cao, C. Li and Q. Ouyang, *ACS Appl. Mater. Interfaces*, 2012, **4**, 6436−6442.

64 J. Hays, A. Punnoose, R. Baldner, M. H. Engelhard, J. Peloquin and K. M. Reddy, *Phys. Rev. B*, 2005, **72**, 075203-1−7.

65 S. Zhuang, X. Xu, Y. Pang, H. Li, B. Yu and J. Hu, *J. Magnet. Magnet. Mater*., 2013, **327**, 24–27.

66 P. Wu, B. Zhou and W. Zhou, *Appl. Phys. Lett*., 2012, **100**, 182405-1–4.

67 M. Venkatesan, C. B. Fitzgerald, J. M. D. Coey, *Nature*, 2004, **430**, 630.

68 A. Roldan, F. Illas, M. Boronat and A. Corma, *J. Phys. Chem. C*, 2010, **114**, 6511–6517.

69 B. Santara, P. K Giri, S. Dhara, K. Imakita and M. Fujii, *J. Phys. D: Appl. Phys*., 2014, **47**, 235304-1–14.

70 Y. K. Kho, A. Iwase, W. Y. Teoh, L. Madler, A. Kudo and R. Amal, *J. Phys. Chem. C*, 2010, **114,** 2821–2829.

71 T. Berger, M. Sterrer, O. Diwald, E. Kno1zinger, D. Panayotov, T. L. Thompson and J. T. Yates Jr., *J. Phys. Chem. B*, 2005, **109***,* 6061–6068.

Figure captions:

Fig. 1 XRD patterns (a) 10-80º, (b) 23-29º and (c) 31-37º of Sn-Ti-x samples, where anatase (A), rutile (R) and casseterite (C).

Fig. 2 Raman spectra of Sn-Ti-x samples at room temperature, where anatase (A) and rutile (R).

Fig. 3 ^{119}Sn Mossbauer spectra of Sn-Ti-x samples at room temperature.

Fig. 4 (a) Survey, (b) Ti 2*p*, (c) Sn 3*d* and (d) O 1*s* XPS spectra of Sn-Ti-0.17 sample.

Fig. 5 EDX spectrum (a), line spectra (b) and mappings (d, e, f) of Sn-Ti-0.05 sample.

Fig. 6 TEM images and selected area electron diffraction patterns of (a) Sn-Ti-0.05, (b) Sn-Ti-0.30 and (c) Sn-Ti-1.37 samples.

Fig. 7 HRTEM images of (a) Sn-Ti-0.05, (b) Sn-Ti-0.30 and (c) Sn-Ti-1.37 samples.

Fig. 8 (a) Repetitive scan spectra of photodegradation of MO in water over Sn-Ti-0.05 sample and (b) PDE of SnO_2, TiO_2 (rutile) and Sn-Ti-x samples vs time under visible light irradiation.

Fig. 9 Repetitive scan spectra of photodegradation of *R*PhOH in water over Sn-Ti-0.05 sample under UV light irradiation (368 nm).

Fig. 10 (a) PDE of PhOH in water over SnO_2, rutile TiO_2 and Sn-Ti-x samples vs irradiation times and (b) relation between PDE and the Hammett substituent constant (σ) of *R*PhOH with the presence of Sn-Ti-0.05 sample under UV light irradiation at 240 min.

Fig. 11 PL spectra of Sn-Ti-x samples at room temperature.

Fig. 12 Magnetic hysteresis loops of Sn-Ti-x samples. (a) x = 0.05 and 0.12 and (b) x = 0.17, 0.30, 1.14 and 1.37 samples at room temperature, the inset gives the enlarged M–H curves between -500 G and 500 G.

Fig. 13 Variation of intensity of emission band, M_r and PDE (phenol degradation) values of Sn-Ti-x with different Sn doping level.

Table 1 The values of particle size (D), band gap energy (E_g) and life time (τ) for Sn-Ti-x samples.

samples	D (nm)	E_g (eV)	life time (ns)			amplitude ($\times 10^{-3}$)			
			τ_1	τ_2	τ_3	a_1	a_2	a_3	χ^2
Sn-Ti-0	27.91	3.30	1.48	10.07	0.22	22.05	1.22	1259.21	1.16
Sn-Ti-0.05	14.48	3.18	2.80	38.29	0.17	12.74	9.70	791.41	1.28
Sn-Ti-0.12	9.54	3.19	2.88	37.37	0.34	17.47	13.32	354.40	1.11
Sn-Ti-0.17	10.60	3.20	2.59	37.74	0.09	7.02	5.54	2056.93	1.21
Sn-Ti-0.30	8.21	3.20	2.71	37.84	0.02	11.17	9.44	924.56	1.32
Sn-Ti-1.14	6.66	3.21	2.39	33.91	0.15	10.58	8.26	983.07	1.12
Sn-Ti-1.37	6.57	3.24	2.53	34.82	0.11	6.99	5.41	1630.39	1.71

Table 2 ^{119}Sn Mössbauer, VSM parameters and PDE values of Sn-Ti-x samples at room temperature.

	MB				VSM			
samples	*IS (mm s^{-1})*	*QS (mm s^{-1})*	*LW (mm s^{-1})*	relative area (*%*)	M_s (memu g^{-1})	H_c (G)	M_r (memu g^{-1})	PDE (%)
Sn-Ti-0	-	-	-	-	10.30	109.33	1.08	42.59
Sn-Ti-0.05	0.14	1.02	2.53	100	16.66	105.33	1.30	70.89
Sn-Ti-0.12	0.14	1.30	2.53	100	129.56	57.12	6.23	68.45
Sn-Ti-0.17	0.10	1.13	2.54	100	0.16	277.13	0.02	57.16
Sn-Ti-0.30	0.13	1.34	2.53	88	0.12	296.71	0.02	7.17
	0.09	4.28	2.53	12	-	-	-	-
Sn-Ti-1.14	0.14	1.65	2.53	73	0.13	821.14	0.04	25.73
	0.12	5.64	2.53	27	-	-	-	-
Sn-Ti-1.37	0.11	1.76	2.53	74	0.10	318.63	0.02	23.39
	0.16	5.86	2.53	26	-	-	-	-

PDE were calculated from photodegradation of phenol in water with Sn-Ti-x samples under ultraviolet light irradiation (368 nm) at 240 min.

Table 3 EDX and BET data for Sn-Ti-x samples.

	EDX, atomic (%)			BET		
samples	Ti	Sn	O	surface area (m^2 g^{-1})	Langmuir surface area (m^2 g^{-1})	pore size (nm)
Sn-Ti-0	33.33	-	66.67	45.80	73.48	25.49
Sn-Ti-0.05	31.49	1.59	66.93	75.42	688.68	8.48
Sn-Ti-0.12	28.49	3.44	68.07	107.43	593.05	5.34
Sn-Ti-0.17	32.09	5.49	62.42	70.98	648.47	7.99
Sn-Ti-0.30	40.04	12.18	47.78	70.92	112.65	13.21
Sn-Ti-1.14	15.49	17.71	66.80	60.82	368.69	5.86
Sn-Ti-1.37	14.15	19.33	66.52	65.89	105.21	6.17

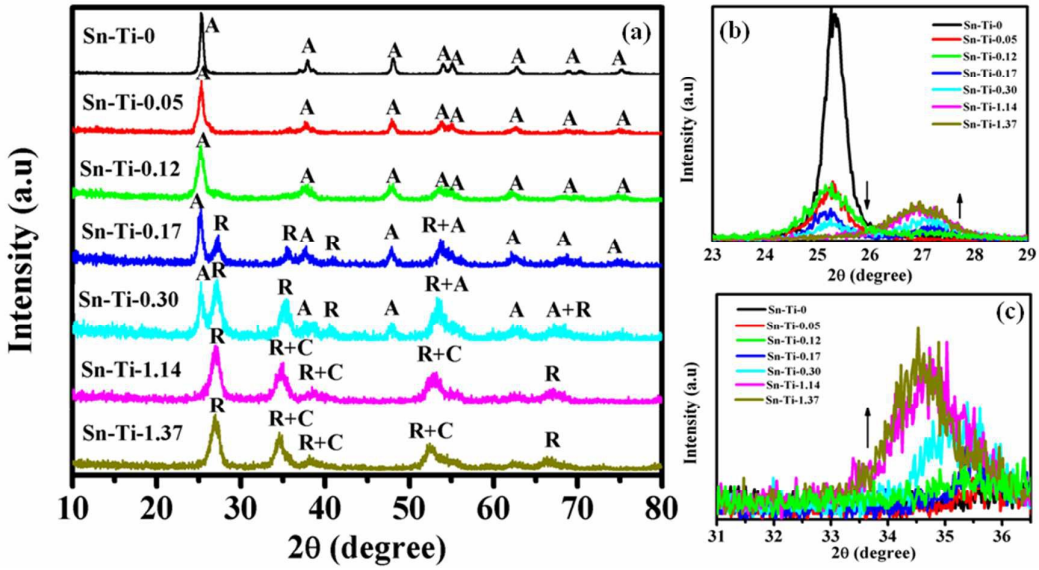

Fig. 1

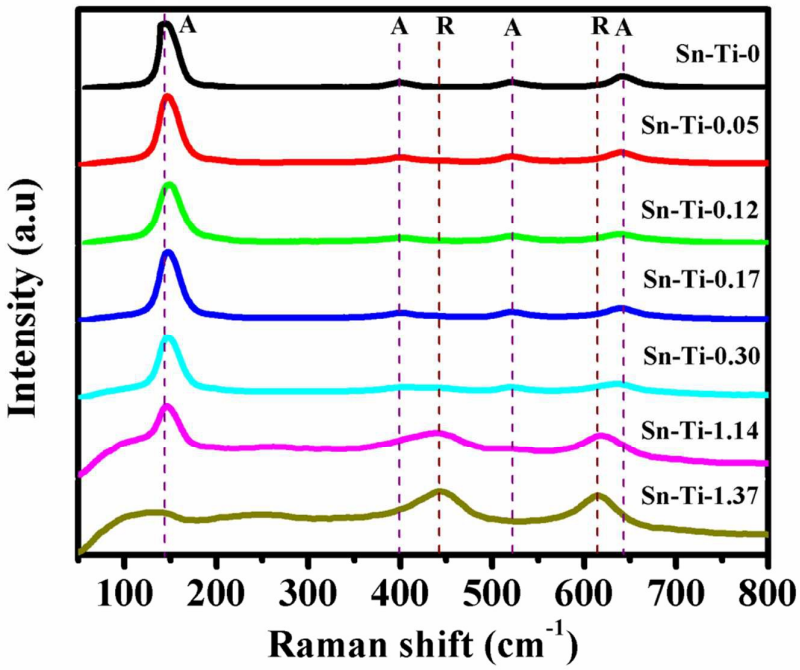

Fig. 2

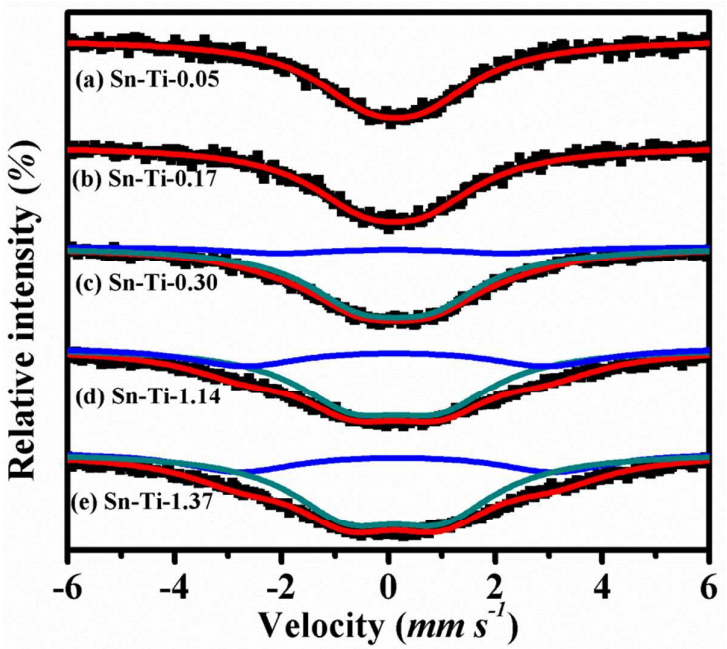

Fig. 3

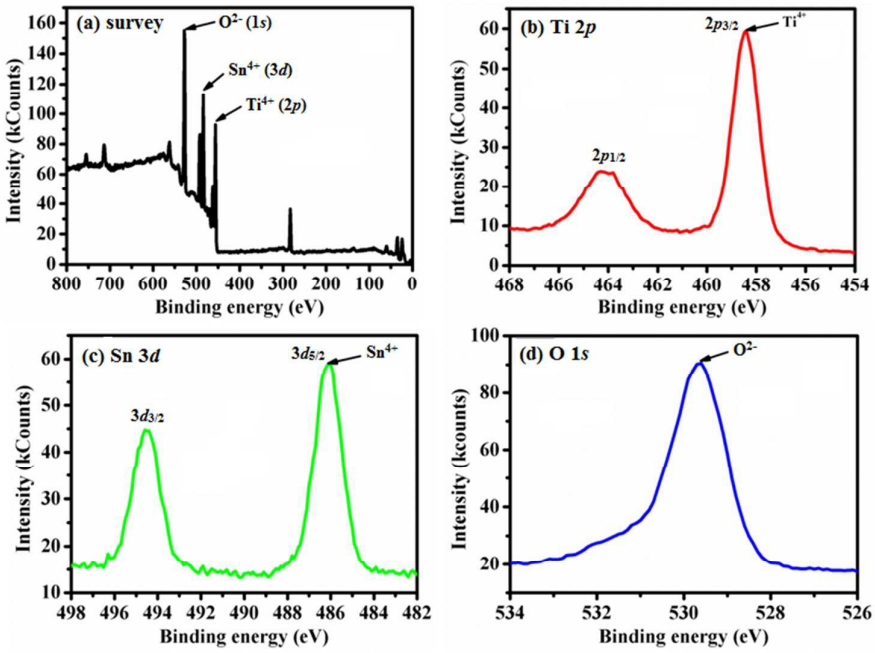

Fig. 4

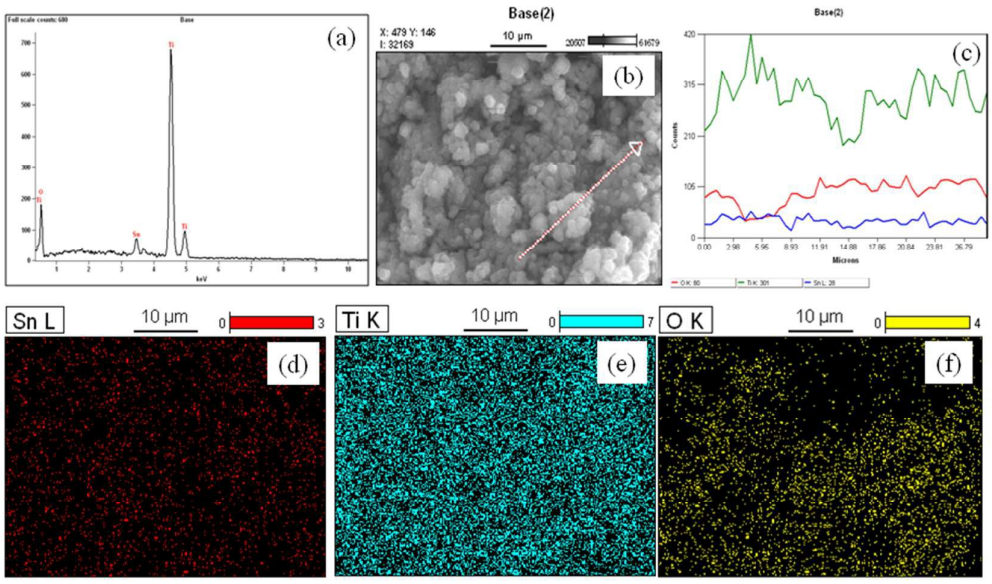

Fig. 5

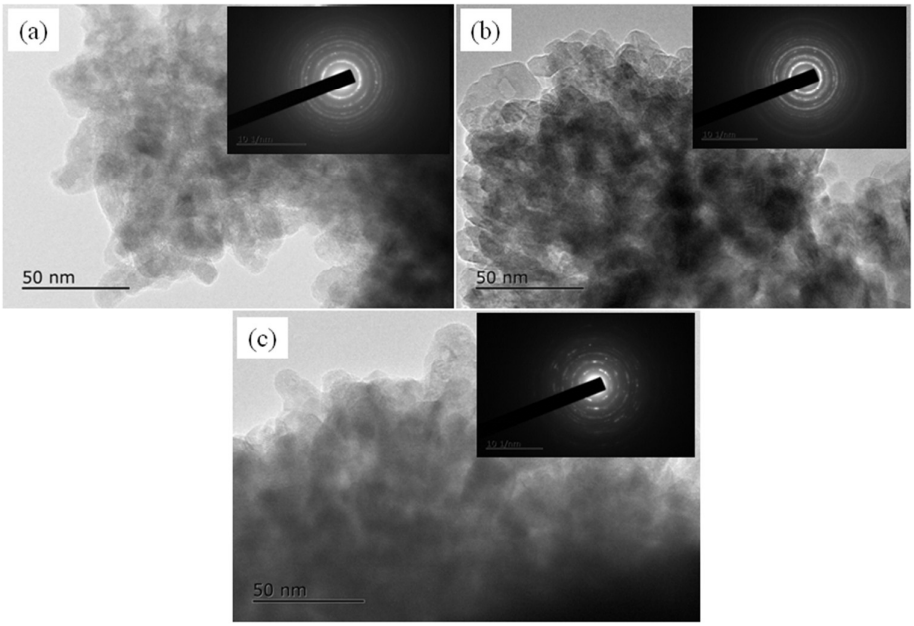

Fig. 6

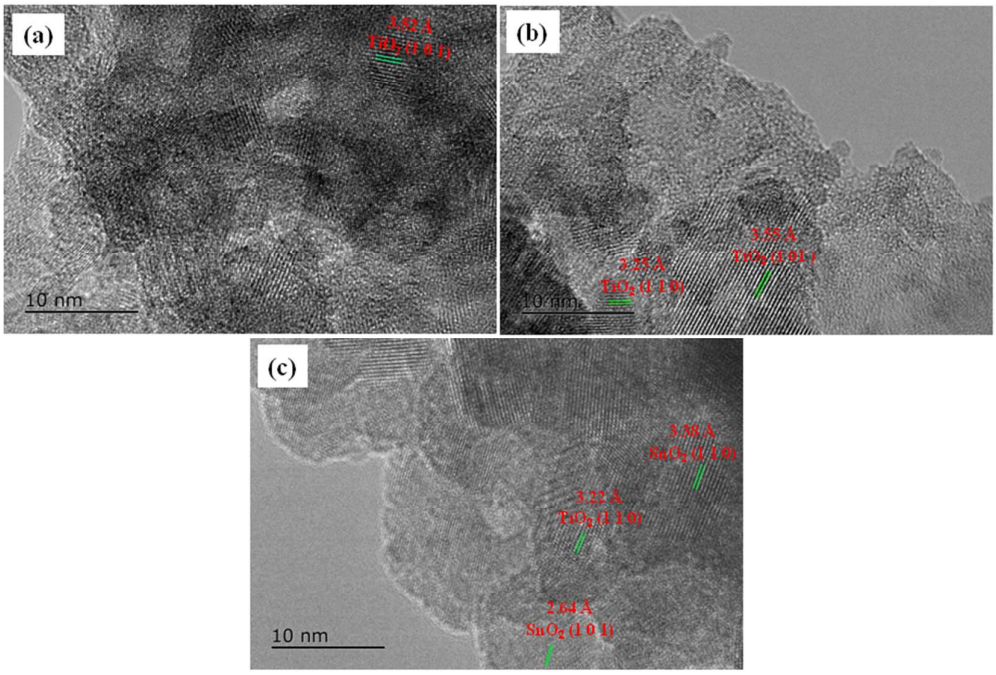

Fig. 7

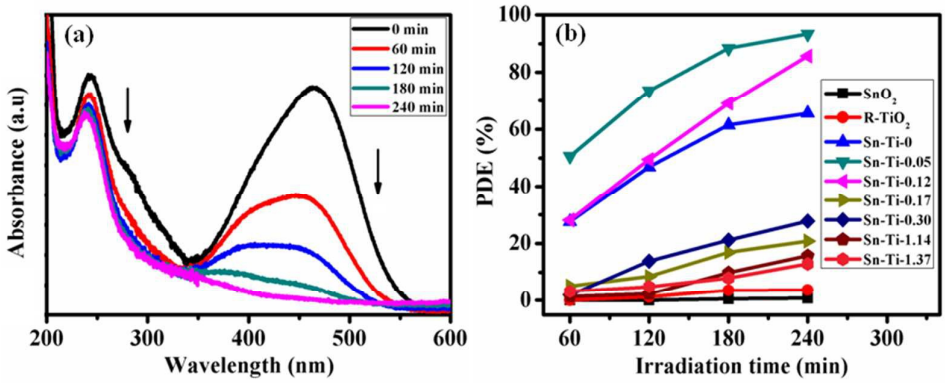

Fig. 8

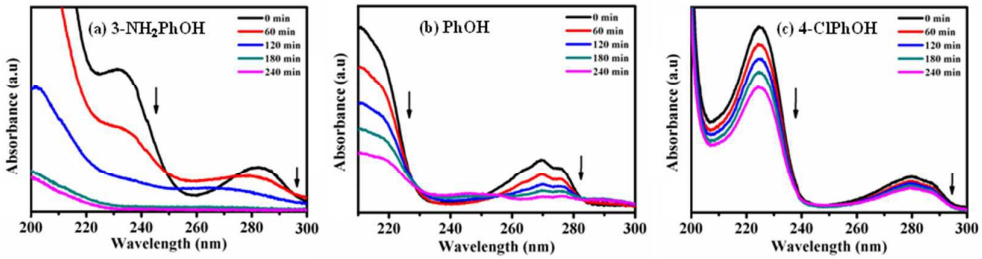

Fig. 9

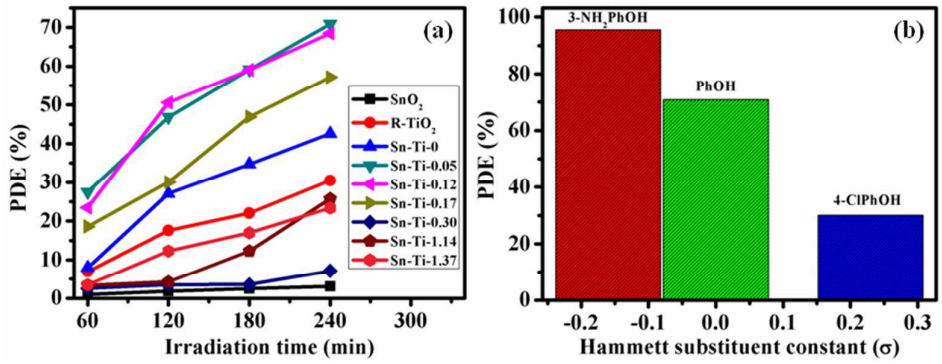

Fig. 10

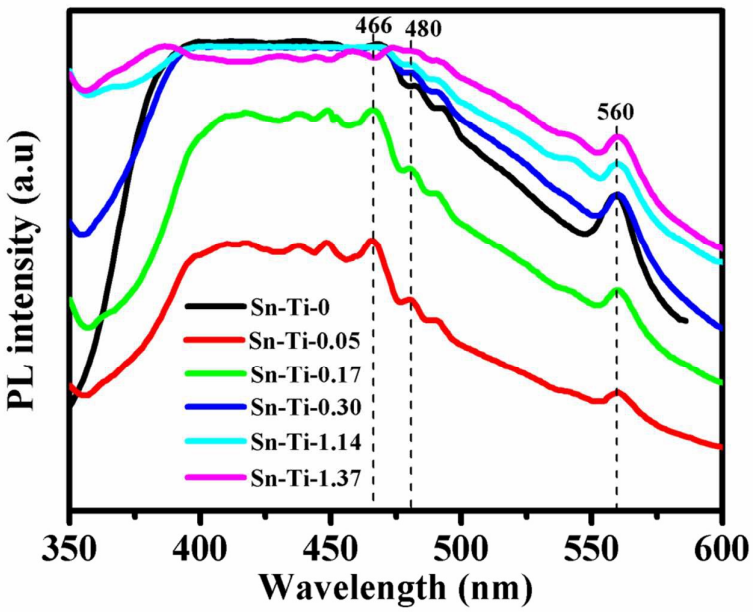

Fig. 11

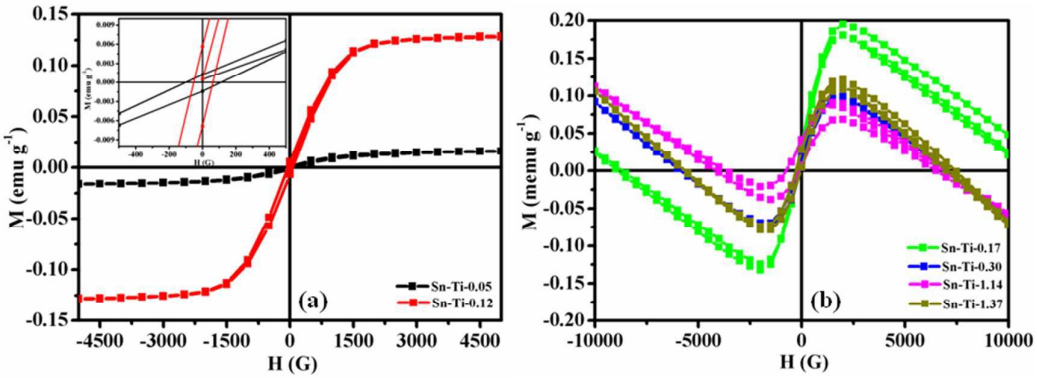

Fig. 12

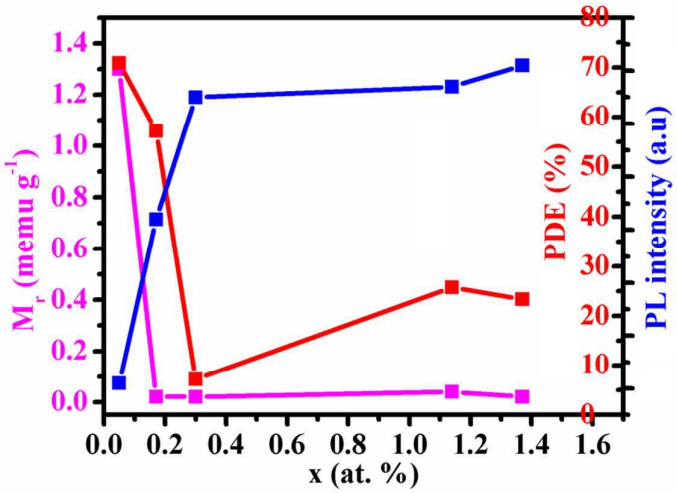

Fig. 13

Graphical Abstract

The ferromagnetic Sn-TiO_2 nanocrystals were newly developed, its photocatalytic activity showed structural, luminescent and magnetic dependences.